

1 Petrography and geochemistry of carbonate rocks of the Paleoproterozoic Zaonega Formation,
2 Russia: documentation of ^{13}C -depleted non-primary calcite.

3
4 A.E. Črne^{a,b}, V.A. Melezhik^a, A. Lepland^{a,c}, A.E. Fallick^d, A.R. Prave^e, A.T. Brasier^{d,f}

5
6 ^aGeological Survey of Norway, Postboks 6315 Sluppen, NO-7491 Trondheim, Norway;
7 alenka.crne@ngu.no, victor.melezhik@ngu.no, aivo.lepland@ngu.no; tel. +4773904482

8 ^bIvan Rakovec Institute of Palaeontology ZRC SAZU, Novi trg 2, SI-1000 Ljubljana, Slovenia

9 ^cTallinn Technical University, Institute of Geology, 19086 Tallinn, Estonia

10 ^dScottish Universities Environmental Research Centre, Scottish Enterprise Technology Park,
11 East Kilbride G75 0QF, Scotland, UK; aef1p@udcf.gla.ac.uk

12 ^eDepartment of Earth and Environmental Sciences, University of St Andrews, St Andrews KY16
13 9AL, Scotland, UK; ap13@st-andrews.ac.uk

14 ^fFaculty of Earth and Life Sciences, Vrije Universiteit Amsterdam, De Boelelaan 1085, 1081HV
15 Amsterdam; a.t.brasier@vu.nl

16
17
18 Abstract

19 The ca. 2.0 Ga Zaonega Formation in the Onega Basin of NW Russia represents a deep-water,
20 mixed siliciclastic-carbonate depositional system with voluminous mafic volcanism. It is typified
21 by extremely organic-rich rocks (TOC > 40 wt%) and represents one of the earliest known
22 episodes of oil/asphalt generation. These rocks have been inferred to archive one of the largest
23 negative $\delta^{13}\text{C}$ excursions in Earth history, one that followed and/or partially overlapped with the
24 2.2–2.06 Ga worldwide Lomagundi-Jatuli carbonate carbon isotopic excursion to high values
25 and thought to be linked to the Paleoproterozoic oxygenation of Earth's surface environments.

26 In order to assess the post-depositional integrity of the carbonate carbon isotopic signal
27 ($\delta^{13}\text{C}_{\text{carb}}$) of the Zaonega rocks, we examined in detail the petrography and geochemistry of eight
28 carbonate beds (0.3 to 0.9 m thick) from different stratigraphic levels of the formation. The range
29 of $\delta^{13}\text{C}$ values for a single bed can be as much as 17 ‰, with calcite being significantly depleted
30 in ^{13}C relative to co-existing dolomite; the ^{13}C -depleted calcite likely formed by involvement of
31 carbon derived from diagenetic and catagenetic alteration of organic matter possibly abetted by

32 volcanic CO₂. The presence of calcite ± talc ± phlogopite ± actinolite indicates metamorphic
33 reaction of dolomite with quartz, or possibly K-feldspar, in the presence of water; commonly
34 accompanied by degassing of ¹³C-enriched CO₂, this caused further ¹³C depletion of newly
35 formed calcite. The least altered dolomite is documented in central parts of thick dolostone beds
36 with variably calcitized margins. This dolomite is considered as the earliest and possibly primary
37 carbonate phase, potentially recording the δ¹³C signal of the ambient seawater. The least-altered
38 dolomite is found in two stratigraphic intervals exhibiting δ¹³C values of +8 and +4 ‰ for the
39 middle part of the formation, and δ¹³C values of -2 and -4 ‰ for the upper part. All other beds,
40 with δ¹³C ranging from -19 to +3 ‰, are considered to have been variably depleted in their ¹³C
41 content by post-depositional processes and therefore cannot be reliably used for assessing the
42 carbon isotope composition of Paleoproterozoic seawater. Our results emphasise the importance
43 of distinguishing primary versus secondary (or later) isotopic compositions in studies of
44 carbonate rocks used for reconstruction of global environmental change.

45
46 Keywords: Paleoproterozoic, carbon cycle, non-primary calcite, Russia, Great Oxidation Event,
47 Onega Basin

49 1. Introduction

50 Ratios of stable carbon isotopes (¹³C/¹²C reported as δ¹³C) in carbonate rocks are widely
51 used for tracking the global carbon cycle and associated environmental conditions as far back in
52 time as the sedimentary rock record exists (Schidlowski, 2001). One of the most profound events
53 of Earth history was the Paleoproterozoic oxygenation of Earth's atmosphere, beginning around
54 2.5 Ga (Bekker et al., 2004; Farquhar et al., 2000). This is marked by a worldwide δ¹³C
55 excursion to high values in carbonate rocks (Baker and Fallick, 1989; Karhu and Holland, 1996),
56 and known as the Lomagundi-Jatuli isotopic event. Genesis of this event has been explained by
57 intensive burial of organic matter and associated accumulation of oxygen in the atmosphere
58 (Karhu and Holland, 1996), although Melezhik and Fallick (1996) have discussed some
59 problems with this idea. The Zaonega Formation was deposited after or partially overlapping
60 with the Lomagundi-Jatuli Event (Hannah et al., 2008) and contains rocks extremely enriched in

61 organic matter (TOC > 40 wt%; Melezhik et al., 1999; 2004). The isotopic compositions of
62 reduced and oxidized carbon from the Zaonega Formation have been used in attempts to
63 reconstruct the global carbon cycle for this important interval of Earth history (Kump et al.,
64 2011; Melezhik et al., 1999; Yudovich et al., 1991). The goal of this study is to perform a
65 detailed petrographic and geochemical study of the carbonate-containing rocks of the Zaonega
66 Formation preparatory to an evaluation of their applicability for reconstruction of
67 Paleoproterozoic sea-water compositions, and consequently, for interpretations of perturbations
68 in the global carbon cycle during Paleoproterozoic time.

69 The sedimentary and volcanic rocks of the Zaonega Formation in Karelia, NW Russia
70 (Fig. 1) were drilled as part of the International Continental Drilling Program's Fennoscandia
71 Arctic Russia - Drilling Early Earth Project (FAR-DEEP). The Zaonega rocks record a mixed
72 siliciclastic-carbonate depositional system, with much magmatic activity contemporaneous with
73 sedimentation (Črne et al., 2013a,b). They also contain one of the earliest known generations of
74 oil/asphalt and proposed hydrocarbon seeps onto the sea floor (Melezhik et al., 2009; Qu et al.,
75 2012; Strauss et al., 2013). The Zaonega Formation and associated rocks experienced regional
76 greenschist facies metamorphism during the 1.8 Ga Svecofennian episode of orogenesis
77 (Volodichev, 1987).

78 Previously-reported carbonate $\delta^{13}\text{C}$ values from the Zaonega Formation range from -25 to
79 +10 ‰ (Krupenik et al., 2011; Kump et al., 2011; Melezhik et al., 1999; Yudovich et al., 1991).
80 Yudovich et al. (1991) interpreted all the ^{13}C -rich carbonate rocks of the Tulomozero and
81 Zaonega formations to be the result of methanogenesis, whereas low $\delta^{13}\text{C}$ values of the Zaonega
82 carbonates were taken as an indicator of both methanotrophy, and a negative isotopic shift in
83 dissolved inorganic carbon due to atmospheric oxidation of biologically produced CH_4 . Krupenik
84 et al. (2011) interpreted all the carbonate rocks to be diagenetically altered to some degree such
85 that the range in carbon isotope values between -1 and -20 ‰ was the result of various
86 proportions of oxidized organic matter being incorporated into early diagenetic carbonate
87 minerals. Most investigations of the Zaonega carbonate rocks highlighted the very low $\delta^{13}\text{C}$
88 and/or $\delta^{18}\text{O}$ values (Krupenik et al., 2011; Melezhik et al., 1999) and/or an exceptionally low
89 $\Delta^{13}\text{C}$ ($\delta^{13}\text{C}_{\text{carbonate}} - \delta^{13}\text{C}_{\text{organic}}$; Kump et al., 2011) to conclude that some post-depositional
90 isotopic overprinting had indeed occurred, but a systematic petrographic and geochemical study
91 to substantiate these inferences has not yet been reported. This paper addresses that shortcoming.

92 The negative $\delta^{13}\text{C}$ excursion recorded in the Zaonega Formation, together with assumed
93 coeval strata in the Francevillian Basin, has been interpreted as one of the largest ever
94 perturbations of the global carbon cycle reflecting intense, oxidative weathering of organic-rich
95 rocks as the result of rising oxygen levels in the atmosphere (Kump et al., 2011). This is an
96 important new hypothesis regarding the manner of Earth's transition to an oxygenated planet and
97 underscores the need to carefully assess the potential modification of primary isotopic signals.
98 Post-depositional alteration of the primary $\delta^{13}\text{C}$ signal may have occurred during diagenesis
99 driven by respiration of organic matter and also later, during contact and regional metamorphic
100 episodes that the Zaonega rocks have experienced. Within the studied depositional basin, locally
101 generated, syn-sedimentary and/or diagenetic hydrocarbon-rich fluids containing ^{13}C -depleted
102 species, including carbonic acid and CH_4 , could have produced secondary carbonates and altered
103 the original carbon isotope composition of primary carbonates. We examined in detail eight
104 representative carbonate beds from cores of the Zaonega Formation, geochemically and
105 petrographically characterizing closely spaced samples within each bed in order to: i)
106 differentiate between early and late carbonate phases and determine their carbon and oxygen
107 isotopic signatures; ii) investigate the potential processes of post-depositional alteration
108 influencing the carbonate carbon isotope record; and iii) estimate the magnitude of any such
109 alteration.

110 **2. Zaonega Formation and the FAR DEEP core material**

111 FAR-DEEP drillholes 12A, 12B and 13A targeted the Zaonega Formation in the Onega
112 Basin of central Karelia, northwestern Russia (Fig. 1). Drillholes 12A and 12B were drilled at
113 the same site, few metres apart (latitude 62.4947 N, longitude 35.2887 E). The reason for the two
114 holes from the same site is that drillhole 12A had to be aborted at the depth of ca. 100 m due to
115 technical problems. Drillhole 12B was drilled without sampling the core for the top 95 m and the
116 correlation between 12A and 12B was made using the lower contact of a large igneous body with
117 the underlying sedimentary rocks occurring at 95.45 m in 12A and 94.56 m in 12B. As these two
118 drillholes provide a continuous rock record, we refer to an integrated drillhole 12AB throughout
119 this article. Drillhole 13A is located approximately 25 km WNW of drillhole 12AB (latitude
120 62.5891 N, longitude 34.9273 E; Fig. 1). During the Paleoproterozoic, the investigated area was

121 part of the rifted flank of the Karelian craton and formed its continental margin to the
122 Svecofennian Ocean (Lahtinen et al., 2008; Melezhik et al, 1999).

123 The Zaonega Formation is a ca. 1500 m thick succession and consists of interbedded
124 sandstones, siltstones, basalts, limestones, dolostones, cherts, and mafic tuffs all of which are
125 intruded by gabbroic sills (Črne et al., 2013a,b; Galdobina, 1987). It occurs above the 400- to
126 800-m-thick Tulomozero Formation, a shallow marine-sabkha succession dominated by
127 carbonate rocks that preserve the Lomagundi-Jatuli isotopic signature (Brasier et al., 2011;
128 Melezhik et al., 2000). The nature of the contact between these two formations is unresolved and
129 interpretations vary from it being either conformable, or an erosional unconformity (Melezhik et
130 al., 2013), or a tectonic contact (Galdobina, 1987). A minimum age for the Zaonega Formation
131 of ca. 1.98 Ga is constrained by several whole-rock and mineral Sm-Nd and Pb-Pb isochrons on
132 a mafic-ultramafic sill of the overlying Suisari Formation (Puchtel et al., 1998; 1999), which is
133 consistent with a Re-Os age of ca. 2.05 Ga obtained on organic matter from the Zaonega
134 Formation (Hannah et al., 2008). The depositional age of the underlying Tulomozero Formation
135 has been constrained by a Pb-Pb age on dolomite of 2.09 ± 0.07 Ga (Ovchinnikova et al. 2007).
136 Termination of the Lomagundi-Jatuli isotope excursion occurred at 2.06 Ga in Finland and Kola,
137 Russia (Karhu, 1993; Martin et al., 2013; Melezhik et al., 2007), but no definite ages exist for the
138 Karelian succession. Thus the maximum-minimum constraints of 2.09 ± 0.07 and 1.98 Ga for the
139 Zaonega Formation indicate its deposition partly overlapped with and/or post-dated the
140 Lomagundi-Jatuli Event.

141 The presence of lavas and gabbroic sills, some with peperite contacts, throughout the
142 entire Zaonega Formation indicates a tectonically and magmatically active depositional setting.
143 Thick intervals of massive organic-rich rocks, commonly associated with mafic lava flows and
144 gabbroic sills, have been interpreted to result from hydrocarbon generation and migration either
145 within the already deposited succession in the form of diapirs (Filippov, 1994) or as
146 hydrocarbon-rich/asphalt spills on the sea-floor (Melezhik et al., 2004; Qu et al., 2012; Strauss et
147 al., 2013). Cavities associated with migrated hydrocarbons provide evidence for generation of
148 fluids, possibly in the form of SO_2 , CO_2 , and/or CH_4 (Qu et al., 2012; Strauss et al., 2013).

149 The succession recovered by the FAR-DEEP cores 12AB and 13A (Fig. 2) was divided
150 into four lithostratigraphic units, from bottom to top, the Greywacke, Dolostone-Greywacke,
151 Mudstone-Limestone, and Dolostone-Chert members (Črne et al., 2013a,b). The major facies

152 change at the boundary between the Mudstone-Limestone and Dolostone-Chert members
153 occurring at 9.3 m in core 12AB and at 76.6 m in core 13A is used for correlating the cores (Črne
154 et al., 2013b). The cored rock represent a deep-water, mixed siliciclastic-carbonate depositional
155 system with voluminous mafic volcanism and turbidity-current deposits represented by flat-
156 laminated, normally graded greywackes interbedded with mudstones, dolostones and limestones;
157 rare debrites are the result of erosion and redeposition within the basin, whereas thick mudstone
158 packages represent background hemipelagic sedimentation (Črne et al., 2013a). Several
159 consecutive intervals of massive organic-rich rocks sandwiched conformably by laminated
160 mudstones (Črne et al, 2013a; 156-133 m in drillcore 12AB; Fig. 2) are interpreted as
161 hydrocarbon-rich/asphalt spills on the sea-floor (Qu et al., 2012; Strauss et al., 2013).

162 Carbonate beds are present throughout the stratigraphy and their abundance, thickness
163 and textural characteristics are distinctive to each lithostratigraphic member. The Greywacke
164 member contains individual, thin beds of sandy limestone that thicken to several decimeters
165 towards the top of the member, where carbonate concretions were recognized (Črne et al.,
166 2013a). Because it is difficult to identify diagenetic carbonate concretions and layers as such if
167 they have lateral dimensions greater than the width of the core, it is possible that they occur in
168 places in the stratigraphy. The depositional mechanism considered to be most likely for the
169 Zaonega primary carbonates, is the shedding of carbonate from the shallow-water environment
170 into the deeper basin. This is supported by a carbonate bed within the Greywacke member,
171 which contains re-crystallized ooids indicating re-deposition of allochems within the
172 Paleoproterozoic Onega Basin. Above this, dolostones and sandy dolostones of the Dolostone-
173 Greywacke member occur as several-metres-thick, flat-laminated layers, or as metre-thick,
174 massive beds. The carbonate beds of the Mudstone-Limestone member are thinner, a few
175 decimetres-thick and indistinctly laminated or massive. The uppermost part of the stratigraphy is
176 typified by thick-bedded massive dolostone. We chose from one to three carbonate beds from
177 each of the members thereby spanning most of the cored Zaonega Formation (Fig. 2).

178

179 **3. Sampling and methods**

180 A total of 39 bulk and 29, 1-2 mm diamond-drilled samples were obtained from eight
181 carbonate beds and analyzed at the Geological Survey of Norway (NGU), the Scottish
182 Universities Environmental Research Centre (SUERC), East Kilbride, Scotland, and at the

183 University of Munster in Germany (Fig. 3; Table A1 in Appendix A). Major and trace elements
184 were analyzed at NGU by X-ray fluorescence spectrometry using a PANalytical Axios at 4 kW
185 and elemental concentrations were determined on acidified extracts (cold 10% HCl acid) by
186 inductively coupled plasma-atomic emission spectrometry (ICP-AES) using a Thermo Jarell Ash
187 ICP 61. Total sulphur (TS), total organic carbon (TOC), and total carbon (TC) were determined
188 at NGU (16 samples) and at University of Munster (23 samples). At NGU sealed tube
189 combustion using a Leco SC-444 had a total analytical uncertainty of 15%. For measurements of
190 TOC, the samples were reacted with 10% HCl acid before the combustion and inorganic carbon
191 (IC) was calculated from TOC and TC. At University of Munster the IC was determined by
192 reactions with 2 N perchloric acid (HClO₄) and TC by combustion of the sample; TOC was
193 calculated from TC and IC. The 29 drilled samples and 39 bulk samples were analyzed for stable
194 carbon and oxygen isotopes at SUERC using conventional procedures. For analyses of stable
195 carbon and oxygen isotopes approximately 1 mg of sample was reacted overnight with
196 phosphoric acid at 70°C and stable carbon and oxygen isotopes ratios were measured on the
197 purified CO₂ using a SIRA II mass spectrometer. Twenty samples were analyzed for stable
198 carbon and oxygen isotope ratios by sequential extraction of CO₂ in two steps. The first step
199 included reaction of several tens of milligrams of sample with phosphoric acid for three hours in
200 a water-bath at 25°C. As a second step, the remaining sample was reacted with phosphoric acid
201 overnight in a hot-block at 100°C. The amount of CO₂ was measured after each step and the
202 carbon and oxygen isotopic composition was measured using a SIRA II mass spectrometer; the
203 precision and accuracy are difficult to specify since they will depend on the efficacy of the
204 sequential extraction procedure and the absolute and relative amounts of different carbonate
205 phases present, but ±0.5 ‰ seems a conservative working estimate (Table A2 in Appendix A).
206 Carbon and oxygen isotopic values are reported and discussed in the conventional delta notation
207 relative to Vienna Pee Dee Belemnite (VPDB).

208 Petrographic characterization of 19 polished thick sections (ca. 200µm in thickness), at
209 least two from each carbonate bed, involved backscattered electron imaging with a scanning
210 electron microscope (SEM-BSE) and the use of cathodoluminescence (CL). SEM-BSE work was
211 done at NGU using an SEM Leo1450VP in low vacuum mode at 16 Pa, an acceleration voltage
212 of 15 kV and a beam of 80 µA. The CL work was done at Karst Research Institute at Postojna,
213 Slovenia, using a CL8200 Mk4 instrument operating at 15 kV beam energy and a 400 mA beam.

214

215 *3.1. Carbon and oxygen isotope analyses of carbonates by sequential extraction*

216 Twenty samples from beds #1 to #7 were analyzed for carbon and oxygen isotopes by
217 sequential extraction of CO₂ in two steps. δ¹³C and δ¹⁸O values were measured for each step of
218 the reaction, after 3 hours at 25°C and after an overnight reaction at 100°C, and marked as δ¹³C₁,
219 δ¹⁸O₁ for the first and δ¹³C₂, δ¹⁸O₂ for the second step. Due to differences in reaction rates of
220 calcite and dolomite (Al-Aasm et al., 1990), we expected the δ¹³C₁, δ¹⁸O₁ and δ¹³C₂, δ¹⁸O₂ to
221 correspond to the isotopic composition of calcite and dolomite, respectively. In order to evaluate
222 whether the data from the two steps can be reasonably considered to correspond to calcite and
223 dolomite, we compared the amounts of calcite and dolomite determined by ICP-AES for each
224 sample with the measured amount of CO₂ extracted after each step.

225 The majority of the calcite-dominated (Mg/Ca<0.1) and dolomite-dominated
226 (Mg/Ca>0.5) samples of the Zaonega Formation show relatively small, up to 2.5 ‰ differences
227 of δ¹³C between the two steps of extraction (Fig. 4; Table A2). Exceptions are the calcite-
228 dominated sample in bed #6 (difference in δ¹³C between the two steps is 5 ‰) and two dolomite-
229 dominated samples from the bed #1 (difference in δ¹³C between the two steps is 4 ‰). The
230 relatively large differences in δ¹³C between the two steps within the samples, where geochemical
231 data suggest a single carbonate phase of either calcite or dolomite, might be due to the
232 extraction-related kinetic isotopic effect but more likely to isotopic heterogeneity of the sample.
233 During dissolution of dolomite-dominated samples, when a small amount of sample reacts
234 during the first step, anomalously ¹³C-depleted CO₂ could be produced due to an extraction-
235 related kinetic effect, the result being a lower δ¹³C₁ value in comparison to the δ¹³C₂. For the
236 calcite-dominated samples a large amount of sample dissolves after the first step (ca. 60 % of the
237 whole sample reacts in 3 hours, Al-Aasm et al., 1990) and therefore the kinetic effect appears
238 unlikely to be the reason for the differences between δ¹³C of the two steps. Differences between
239 δ¹³C₁ and δ¹³C₂ can also occur in either a dolomite- or calcite-dominated sample, if isotopic
240 heterogeneities are coupled with differences in dissolution rates, e.g. an Fe-poor calcite/dolomite
241 has a different isotopic composition than Fe-rich calcite/dolomite.

242 Based on our dataset and published reaction rates for calcite and dolomite at different
243 temperatures (Al-Aasm et al., 1990), we conclude that the results of the two-step sequential
244 extraction method may be used as an approximation of carbon and oxygen isotope signatures of

245 calcite and dolomite for those samples that contain significant relative amounts of each mineral
246 phase (>5 wt% of all carbonate). Predominance of either of the two mineral phases results in a
247 mixed signal in either of the two steps, complicating the determination of the isotopic differences
248 between calcite and dolomite. We have therefore interpreted the $\delta^{13}\text{C}_1$, $\delta^{18}\text{O}_1$ and $\delta^{13}\text{C}_2$, $\delta^{18}\text{O}_2$ to
249 represent calcite and dolomite respectively for the samples with the following characteristics: i)
250 general correspondence between amounts of calcite and dolomite determined by ICP-AES and
251 the measured amount of CO_2 extracted at each step; and ii) presence of a significant relative
252 amount of each mineral phase (>5 wt% of all carbonate). Other results of the sequential
253 extraction method on the Zaonega samples can be used for determination of isotopic
254 homogeneity of the samples and/or for assessment of the applicability of the method for the
255 Zaonega carbonates. Large differences in $\delta^{13}\text{C}$ between the two steps for the samples containing
256 either pure calcite or pure dolomite imply a limited applicability of the sequential extraction
257 method for all the samples of the Zaonega Formation such that an isotopic variability a few per
258 mil of needs to be taken into account.

259
260

261 **4. Results**

262 The aims of detailed sampling, geochemical analyses and petrographic characterization were: i)
263 assessment of $\delta^{13}\text{C}$ variability within single carbonate beds; and ii) determination of mineralogy
264 and textures of carbonate phases and associated minerals. Geochemical results include analyses
265 of 39 samples for stable carbon and oxygen isotopes, TOC/IC, ICP-AES, and XRF for eight
266 carbonate beds, together with the 29 additional closely spaced samples analyzed only for carbon
267 and oxygen isotopes. The textural characterization of carbonate minerals is based on SEM-BSE
268 and CL images of thin sections. Individual samples represent 12-cm-long quarters of the core
269 taken continuously along the whole thickness of carbonate beds, while one bed (#5) was sampled
270 from core to top. The positions of sample points in Figures 3 and 4 correspond to the tops of
271 individual 12-cm-long samples. The response of carbonate beds to 5 % HCl was monitored
272 during core logging: blue-colored lithologies in Figures 3 and 4 mark intensive reactions whereas
273 violet-coloring indicates lithologies that did not react to the acid (in Figs. 3 and 4).

274

275 *4.1. Geochemistry*

276 Selected geochemical parameters plotted along eight carbonate beds are presented in
277 Figure 3, and results from the carbon and oxygen analyses by sequential extraction are shown in
278 Figure 4. Beds #1 to #6 are described together because they show similar within-bed $\delta^{13}\text{C}$
279 variability of several per mil, with middle portions having relatively higher $\delta^{13}\text{C}$ values
280 compared to the margins (exception is bed #3). Beds #7 and #8 have low within-bed variation of
281 $\delta^{13}\text{C}$ (≈ 2 ‰), hence their geochemical characteristics are described separately.

282

283 Beds #1 to #6

284 The $\delta^{13}\text{C}$ variability within these six, single beds ranges from 4 ‰ (bed #3) to 17 ‰ (bed
285 #6; Fig. 3). All beds, except #3, display a decline in $\delta^{13}\text{C}$ values from their central parts (from -9
286 to +8 ‰; Table 1) outward to their margins (from -19 to -4 ‰; Table 1). For bed #3, the lowest
287 $\delta^{13}\text{C}$ values occur at the base (-8 ‰) and increase consistently upward through the middle (-5 to -
288 6 ‰) and to the top (-4 ‰). $\delta^{18}\text{O}$ values only show minor variation throughout the beds, with
289 beds #1 and #6 having $\delta^{18}\text{O}$ a few per mil higher in their middle parts relative to their margins.
290 Middle parts of all beds contain higher wt% of carbonate (IC=10–11 wt%), and therefore lower
291 wt% of siliciclastic material in comparison to the bed margins. The main carbonate mineral in
292 the central part of the beds is dolomite, which is Fe-Mn-rich in beds #2 to #5 but Fe-Mn poor in
293 beds #1 and #6 (Fig. 3). Calcite prevails at the margins of all beds (exception is lower margin of
294 bed #1), coinciding with relatively low IC and $\delta^{13}\text{C}$ in comparison to the centres of the beds.
295 Calcite contains higher amounts of Sr, up to 320 ppm, in comparison to dolomite with Sr content
296 below 100 ppm; an exception is dolomite in bed #3 with Sr values up to 160 ppm.

297 Whole-rock content of Ca is mostly stable throughout bed thickness, the exception being
298 the upper margins of beds #3 and #6, which are considerably lower in Ca abundance. Mg whole-
299 rock content decreases either significantly (beds #3, #4, #5, #6) or slightly towards the bed
300 margins (beds #1 and #2), broadly matching the trend of IC and $\delta^{13}\text{C}$ (exceptions are margins of
301 beds #1 and #3). The majority of beds with Fe-Mn-rich dolomite in the centres, (beds #2 and #5),
302 contain Fe-Mn-rich calcite at the bed-margins; Fe-poor, Mn-rich calcite is present at the margin
303 of bed #4 and Fe-Mn-poor calcite at the margin of bed #3. Beds #1 and #6, having Fe-Mn-poor
304 dolomite in their centre, also contain Fe-Mn-poor calcite at their margins.

305

306 Beds #7 and #8

307 The main characteristic of these two beds is that there are no significant differences in
308 geochemical compositions from their centres to margins (Fig. 3). The $\delta^{13}\text{C}$ variability is 2 ‰ in
309 bed #7 and 0.3 ‰ in bed #8. The $\delta^{18}\text{O}$ values are stable in both beds (ca. -17 ‰ in bed #7 and -
310 18.5 ‰ in bed #8). Amounts of carbonate and siliciclastic material are stable in bed #8 and
311 inversely proportional in bed #7, ranging from 7 to 10.4 wt% IC and from 7 to 21 wt% SiO_2 . The
312 main carbonate phase in both beds is calcite with Sr content below 110 ppm, which is
313 significantly lower than the Sr content of calcite in beds #1 to #6. Whole-rock content of Mg is
314 low, only a few wt%.

315

316 *4.2. Textural properties of carbonate minerals*

317 Petrographic studies were performed to identify the carbonate components, characterize
318 their microtextures and interrelationships, and assess genetic associations with other mineral
319 phases. At least two thin sections were studied from each of the eight beds, one from the centre
320 of the bed and the other close to the margin of the bed. Samples were characterized by SEM-BSE
321 (hereafter BSE) imaging and cathodoluminescence (Figs. 5, 6 and 7). The beds with common
322 textural properties are described together: i) beds #2 to #5 contain zoned Fe-Mn-rich dolomite;
323 ii) beds #1 and #6 contain homogenous Fe-Mn-poor dolomites; iii) beds #7 and #8 contain low-
324 Sr calcite.

325

326 *Beds #2 to #5*

327 The middle parts of these beds contain zoned dolomite crystals ca. 20 μm in size, either
328 in tightly intergrown indistinct rhombohedral shapes and zones (beds #2 to #4; Figs. 5a, 5d and
329 5g) or rather loosely packed but well-defined rhombohedra with distinct zones; the latter is
330 cemented by dolomite (bed #5; Fig. 5j). Using CL, dolomite is nonluminescent in all samples
331 (e.g. Fig. 5f), only in bed #5 do rhombohedral rims and very few cores show bright red
332 luminescence (Fig. 5l). A significant amount of calcite, in places intergrown with quartz (bed #3;
333 Fig. 5d) and overgrowing dolomite or infilling spaces in partially dissolved dolomite, is present
334 in the middle parts of beds #2 to #4; these beds also contain abundant mica (mostly phlogopite;
335 talc is present in bed #2) and pyrite formed at different stages of diagenesis/metamorphism (Figs.
336 5b and 5d).

337 The margins of these beds contain mostly calcite occurring as smaller (beds #2 and #4) or
338 larger (bed #3), irregularly shaped patches usually intergrown with either quartz (bed #2 and #3;
339 Figs. 5b and 5e) or albite (bed #4; Fig. 5h). Albite occurs also as larger grains/patches, which
340 could be of detrital origin or a product of albitization of older grains, for example plagioclase or
341 sulfide. Dolomite is only present in the margin of bed #5 which contains mostly Ca and Fe-rich
342 dolomite as cement around the dolomitic rhombohedra and some calcite (Fig. 5k). Under CL,
343 calcite luminesces orange with a moderate to bright intensity (e.g. Figs. 5c and 5i). Micas in beds
344 #3 to #5 and talc in bed #2 are more abundant near bed margins than in the centre of the beds.

345

346 Beds #1 and #6

347 The middle parts of these two beds show large, tightly intergrown dolomite crystals ca.
348 70 μm in size (Figs. 6a and 6e); in bed #6, the crystals are so tightly packed that their shapes are
349 difficult to recognize, and only in places are rhombohedra observed. Dolomite crystals are
350 mostly homogeneous in BSE imagery with slightly darker cores in comparison to the outermost
351 parts (the transition is gradual). The contacts between crystals are straight to sutured (Fig. 6e).
352 Under CL most dolomite crystals show very dull red luminescence, some have dull luminescent
353 cores and bright rims, and in bed #1 a few crystals show bright-dull-bright zoning (Fig. 6c).
354 Calcite, mica and talc are present, but in minor amounts in comparison to the margins of the
355 same beds.

356 The lower margin of bed #1 mostly contains dolomite, whereas calcite is the dominant
357 carbonate mineral at the margin of bed #6. The former displays large dolomite crystals ca. 70 μm
358 in size and mostly tightly intergrown with recognizable rhombohedral shapes (Fig. 6b). Inner
359 parts of the crystals are brighter in BSE images in comparison to their outer parts (Fig. 6b).
360 Under CL, dolomite crystals are mostly zoned (dull-bright-dull luminescence), but many are dull
361 with bright rims (Fig. 6d). Where dolomite crystals are less tightly packed, micas and organic
362 matter occur in the interstices. Minor amounts of calcite are present. The margin of bed #6
363 contains calcite intergrown with quartz (dolomite is not observed, Fig. 6f). Talc and phlogopite
364 are more abundant at the margin than at the centre of the bed.

365

366 Beds #7 and #8

367 Bed #8 contains large (ca. 100 μm in size) patches of irregularly shaped calcite with
368 numerous embayments, tightly intergrown with albite (Fig. 7d). The middle part of bed #7
369 contains ca. 20 μm -large BSE homogeneous calcite crystals with albite intercalations; boundaries
370 between the crystals are straight and undulate (Fig. 7a). Albite, micas (phlogopite, chlorite) and
371 titanite are present in both beds, with albite occurring as spherical inclusions within calcite and
372 as rectangular grains in bed #7 (Fig. 7a) and as a mineral phase intergrown with calcite in bed #8
373 (Fig. 7d). Micas overgrowing calcite are more abundant in bed #8. Disseminated titanite is
374 present in both beds. Actinolite is only present in bed #8, overgrowing all mineral phases. Under
375 CL, calcite in both beds has medium-dull red luminescence, but a few small areas are bright red
376 (Fig. 7c).

377 The upper margin of bed #7 contains up to 0.5 mm large rhombohedra having a calcitic
378 core and an outer rim of calcite (Fig. 7b). The calcite forming the core is homogenous in BSE
379 images and contains spherical inclusions of albite of a few μm in size (Fig. 7b). The calcitic rim
380 contains spherical inclusions of quartz a few μm in size. Numerous inclusions of quartz mark the
381 sharp, but undulated boundaries between the core and rim (Fig. 7b). The outer boundary of the
382 calcitic rim to the surrounding quartz matrix is irregular with numerous embayments. Titanite
383 occurs predominantly together with micas in the quartz matrix, but also in the calcite rims and in
384 the cores of the rhombohedra. Micas overgrow all mineral phases.

385

386 5. Discussion

387 5.1. Primary and secondary carbonate precipitates – textural and geochemical indications

388 On the basis of geochemical data, four main carbonate phases have been identified: i) Fe-
389 Mn-poor dolomite (bed #1 and centre of bed #6) and; ii) Fe-Mn-rich dolomite (centres of beds #2
390 to #5); iii) calcite, relatively rich in Sr (hereafter Sr-rich calcite; margins of beds #1 to #6); and
391 iv) calcite relatively poor in Sr (hereafter Sr-poor calcite; beds #7 and #8). Geochemical and
392 textural properties of these four carbonate phases, relevant to their relative order of formation,
393 are discussed below (overview of textural properties is shown in Figs. 8a-n).

394 The Fe-Mn-poor dolomite consists mostly of ≈ 70 μm -large homogenous crystals, which
395 are very tightly intergrown and have a dull red luminescence under CL; only a few crystals
396 (middle part of bed #1) have clearly distinguishable dull red cores and bright red rims under CL
397 (Fig. 6c). Homogenous textures of the Fe-Mn-poor dolomite crystals imply stable conditions

398 during their precipitation in the sedimentary/early diagenetic environment and/or during burial
399 recrystallization. Tight crystal intergrowth, likely developed during burial, could have prevented
400 intensive infiltration of later fluids. The Fe-Mn-poor dolomite is overgrown by texturally later
401 Sr-rich calcite.

402 The Fe-Mn-rich dolomite consists of ≈ 20 μm large, zoned rhombohedral crystals, which
403 are mostly nonluminescent under CL; only a few crystals (bed #5) show bright red luminescent
404 rims and very few of them possess also luminescent cores. Nonluminescence under CL is
405 presumed to be due to quenching by iron in these cases (Machel, 2000). Zoned crystals indicate
406 variable geochemical conditions during precipitation, either due to a closed system as the pore
407 waters are progressively depleted in certain species, or due to infiltration of fluids with a
408 different geochemical signature. The Fe-Mn-rich dolomite is overgrown by the Sr-rich calcite,
409 indicating relatively early formation of Fe-Mn-rich dolomite in relation to the calcite.

410 The Sr-rich calcite in beds #1 to #6 forms irregular patches containing either albite or
411 quartz inclusions and overgrows both types of dolomite in the centres of the beds; this calcite
412 thus formed relatively late with respect to dolomite. The amount of Sr-rich calcite varies along
413 the thickness of each bed, being least at the centres of the beds and greatest at the bed-margins:
414 at the margins of beds #2, #3, #4, and #6, we find only calcite. While the timing of calcite
415 precipitation is more difficult to verify at the bed margins because only one carbonate phase is
416 present, we interpret the calcite at the centres and at the margins of the same beds as an identical
417 phase due to textural similarities (Figs. 5-7). The $\delta^{13}\text{C}$ values of Sr-rich calcite in the studied
418 beds are between -19 ‰ and -4 ‰ (samples with $\text{Mg}/\text{Ca} < 0.1$ in Fig. 8a), which is as much as 17
419 ‰ lower in comparison to the dolomite-dominated samples occurring within the same beds
420 (Figs. 3, 4, 8a). Significantly different carbon isotope composition, and relatively late formation
421 of Sr-rich calcite in comparison to dolomite implies different conditions for the dolomite and Sr-
422 rich calcite formation. This, together with the co-occurrence of calcite with secondary albite and
423 quartz, suggests that the Sr-rich calcite formed later in the post-depositional history of these
424 rocks than the dolomite.

425 The Sr-poor calcite does not occur in conjunction with any other carbonate phase, making
426 it difficult to assess its place in the paragenetic sequence. Texturally, however, the Sr-poor
427 calcite in beds #7 and #8 is comparable to the Sr-rich calcite on the outer margins of beds #1 to
428 #6; i.e. mostly irregularly shaped calcite patches inter-grown with either quartz or albite. Further,

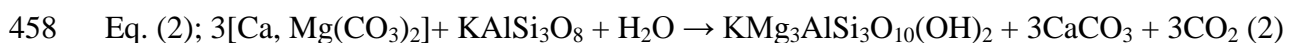
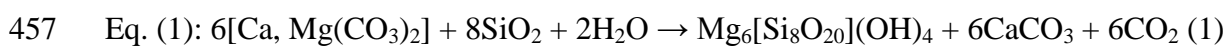
429 the Sr-poor calcite is associated with actinolite in bed #8, which is located 20 m above a 70-m-
430 thick mafic intrusion (Fig. 2). It is most probable that the Sr-rich and Sr-poor calcite formed
431 under similar conditions, the Sr-poor calcite probably at higher temperatures as indicated by the
432 presence of actinolite, implying precipitation of the Sr-poor calcite later than the dolomite.
433 Rhombohedral calcite patches in bed #7 (Fig. 7b) could have formed through complete
434 calcitization of dolomite rhombohedra. The large size of the former suggests their initial
435 formation, or recrystallization, during burial and a later formation of Sr-poor calcite. Small Sr-
436 poor calcite crystals in the centre of bed #7 have well preserved crystal boundaries and likely
437 represent the least altered sedimentary calcite. The $\delta^{13}\text{C}$ and $\delta^{18}\text{O}$ values of all Sr-poor calcite,
438 however, are low and fall within the range of the $\delta^{13}\text{C}$ and $\delta^{18}\text{O}$ values of the Sr-rich calcite (Fig.
439 8d), inferred to reflect post-depositional formation or alteration of earlier carbonates. It is
440 therefore most probable that the small calcite crystals in bed #7 are also of post-depositional
441 origin, or at least their carbon and oxygen isotopic composition have been reset. There may be
442 some primary calcite in bed #7, but the carbon isotope composition of this bed ($\delta^{13}\text{C} = -11 \text{‰}$)
443 and co-occurrence of calcite with albite or quartz is similar to the clearly post-depositional
444 calcite in other beds.

445 In summary, dolomites of both types likely represent primary or early diagenetic
446 carbonate precipitates within the Zaonega Formation, whereas calcite mostly formed as a
447 relatively late carbonate phase precipitating under variable post-depositional, including
448 hydrothermal conditions. This latter interpretation is based on the observation that, within the
449 same samples, calcite overgrows dolomite and has textural association with secondary quartz and
450 albite.

451

452 5.2. Formation of secondary carbonates

453 The calcite \pm talc \pm phlogopite \pm actinolite paragenesis observed in carbonate beds indicates that
454 the following volatilization reactions could have been the pathway influencing $\delta^{13}\text{C}$ and $\delta^{18}\text{O}$
455 composition of residual dolomite and newly formed calcite (Bucher and Frey, 2002; Shieh and
456 Taylor, 1969):



459

460 The CO₂ produced by such reactions can be enriched in ¹³C and ¹⁸O in comparison to the original
461 dolomite due to equilibrium isotopic fractionation between CO₂ and dolomite (Shieh and Taylor,
462 1969; Valley, 1986), and in high-temperature greenschist metamorphic conditions the δ¹³C of the
463 calcite produced was found to be up to 4 ‰ lower than the co-occurring dolomite (e.g. Melezhik
464 and Fallick, 2003; Melezhik et al., 2003). The mineralogy of carbonate beds #1 to #6 is
465 consistent with such alterations, containing reactants (dolomite, quartz) and all the products
466 (phlogopite, talc, and calcite). The reason for the lack of K-feldspar in carbonate beds could be
467 its initial absence, or could be due to complete reaction of K-feldspar with the co-occurring
468 dolomite. Mineral associations together with ¹³C-depletion of calcite imply that Sr-rich calcite
469 formed as a metamorphic reaction product as described by the equations above. The magnitude
470 of δ¹³C depletion of calcite relative to dolomite is as much as 17 ‰. This cannot be due to
471 volatilization alone and requires a ¹³C-depleted fluid to explain the low δ¹³C values of the calcite
472 (Valley, 1986). It is known that large changes in the carbon and oxygen isotope compositions of
473 carbonate rocks can be due to extensive fluid-rock interaction at low metamorphic temperatures
474 (e.g. Guerrera et al., 1997). As the deposition of the Zaonega rocks was accompanied by
475 contemporaneous vigorous magmatic activity, formation of peperites, oil generation and seeping
476 and spilling of hydrocarbons (Črne et al., 2013a,b; Melezhik et al., 2009; Qu et al., 2012), it is
477 reasonable to infer that intense hydrothermal fluid circulation supplied water, silica, CO₂ (likely
478 as carbonic acid) and CH₄ to the depositional system (Strauss et al., 2013).

479 There are abundant possible ¹³C-depleted sources within the Zaonega Formation:
480 volcanic CO₂ with assumed δ¹³C ca. -5 ‰, ample organic matter with δ¹³C between -25 and -42
481 ‰ (Filippov and Golubev, 1994; Kump et al., 2011; Qu et al., 2012) and its catagenetic products
482 (including organic acids and biogenic methane), and inferred thermogenic methane (Qu et al.,
483 2012) with δ¹³C likely between -20 and -50 ‰ (for precursor organic carbon at -25 ‰)
484 (Whiticar, 1999). Although volcanic CO₂ might have played an important role in hydrothermal
485 fluids, it does not in any clear way facilitate precipitation of calcite with δ¹³C values lower than -
486 5 ‰. Oxidation of organic matter forming CO₂ or bicarbonate must have occurred in order to
487 explain the very low δ¹³C values of the secondary calcite. No measured δ¹³C of secondary
488 carbonate demands the involvement of oxidized CH₄, although we recognize that it is
489 geologically reasonable that both biogenic and thermogenic methane were available at various
490 times. Sedimentary rocks within the drilled succession are rich in TOC; mudstones, which are by

491 far the most abundant lithology encompassing the studied carbonate beds in FAR-DEEP cores
492 12AB and 13A, may contain more than 20 wt% of TOC (Črne et al, 2013a,b).

493 Decomposition of organic matter can be facilitated by thermochemical and bacterial
494 processes of sulfate, iron, or manganese reduction, all plausibly sourced from minerals within the
495 Tulomozero and Zaonega formations, and from seawater; H₂O itself is a likely source of oxygen
496 once the oil window is reached. The sulfur isotope data from the Zaonega (Shatsky, 1990) and
497 Pilgugarvi Formations (Melezhik et al., 1998), the latter a unit on the Kola Peninsula that is
498 broadly correlative to the Zaonega Formation (Hannah et al., 2006), indicate presence of sulfate
499 in contemporaneous sea-water enabling sulfate reduction during deposition (Reuschel et al.,
500 2012). Sulfate may have also been supplied from the underlying Tulomozero Formation
501 containing abundant calcitized sulfates (Brasier et al., 2011; Melezhik et al., 2005) and even
502 thick anhydrite beds (Morozov et al., 2010). As the formation of ¹³C-depleted calcite occurred
503 relatively late in comparison to the earlier formed dolomite (that was probably of sedimentary
504 and/or early diagenetic origin), it is likely that low ¹³C carbon was supplied from different depths
505 during burial of the Zaonega sediments (cf. Irwin et al., 1977), followed by metamorphic
506 reactions and possible hydrothermal alterations. Whatever the source of the oxidants and
507 whatever the processes of oxidation, the solid organic matter or fluid hydrocarbons of the
508 Zaonega Formation had ample opportunity to be oxidized and supply ¹³C-depleted CO₂ to the
509 post-depositional fluids.

510 The isotopic uniformity of carbonate beds #7 and #8, located in proximity to thick mafic
511 bodies, is tentatively interpreted to be the result of homogenization of δ¹³C and δ¹⁸O due to
512 pervasive post-depositional fluid infiltration associated with those intrusions. A somewhat
513 similar isotopic effect was reported by Frauenstein et al. (2009) from dolostones in near contact
514 with the Bushveld intrusive complex. The absence of talc within beds #7 and #8 could reflect the
515 actions of pervasive CO₂-rich fluid flow and/or high temperatures (>450 °C) within the lower
516 part of the succession, hindering talc formation and preservation (e.g. Bucher and Frey, 2002).
517 Alternatively, bed #7 may represent either a sedimentary layer or an early diagenetically formed
518 concretion with an original calcitic mineralogy, though (as with all carbonates here) now likely
519 recrystallised.

520 We interpret the pervasive calcitization of the margins of carbonate beds #1 to #6 as
521 caused by: i) reactions between quartz-rich mudstone and dolomite in the presence of

522 hydrothermal fluids; and ii) potential early lithification of the carbonates relative to the organic-
523 rich mudstones resulting in differences in permeability between the two lithologies, thus
524 channeling fluid flow at lithological boundaries. A larger amount of secondary calcite at the bed
525 margins fits a hypothesis of flow of post-depositional fluids along lithological contacts. The
526 intensity of rock-fluid interaction can be approximated by differences in composition between
527 newly formed calcite and its presumed dolomite precursor, up until the point of total resetting. In
528 beds #3 and #4, the calcite is Fe-Mn-poor even though the dolomite within the same bed is Fe-
529 Mn-rich. This can be interpreted as due to greater fluid mobilization in this part of the
530 stratigraphy: both beds are located in close proximity to asphalt spills (Fig. 2; bed #3 is also
531 closer to the magmatic body). High amounts of Fe and Mn in dolomite and calcite in beds #2 and
532 #5 suggest a partly inherited geochemical signature of calcite from its dolomite- precursor and
533 therefore imply less intense fluid mobility and/or interaction in this part of the succession. Less
534 prone to secondary overprints were those carbonate beds that: i) contain tightly intergrown
535 dolomite crystals that inhibited pervasive fluid infiltration; and ii) have the highest initial
536 carbonate content, thereby buffering the carbon isotopic system to a larger degree ($\delta^{13}\text{C}$ is
537 correlative to IC, see Fig. 8c). Noteworthy, though, is that all studied samples show variable
538 signs of alteration as evidence that even the ‘best’ samples (in terms of preserving
539 original/primary carbonate geochemical signatures), contain secondary calcite (e.g. BSE image
540 of the sample from the centre of bed #6 shown in Fig. 6e).

541 Regional greenschist metamorphism at 1.8 Ga could have additionally altered the
542 geochemistry of the Zaonega carbonate rocks. The Zaonega Formation as a whole underwent
543 low- to middle-temperature greenschist-grade regional metamorphism with temperatures of 300
544 to 350°C (Volodichev, 1987); the presence of actinolite (bed #8) indicates locally higher
545 temperature conditions close to the mafic intrusions. Secondary actinolite and albite-calcite
546 intergrowth in proximity to contacts with peperites implies formation of these minerals in
547 relation to mafic intrusions and therefore prior to complete lithification. It is therefore likely that
548 some calcite formed locally as a secondary mineral of hydrothermal/metasomatic origin before
549 the regional metamorphic event, while some might have formed earlier, perhaps during early
550 (syn-sedimentary?) diagenesis (e.g. bed #7), and we do not entirely exclude a possible initial
551 calcitic mineralogy of some carbonate beds.

552 In summary, the lower part of the Zaonega succession might have experienced extensive
553 fluid circulation causing complete calcitization of carbonate beds, although their original calcite
554 mineralogy cannot be excluded. In the upper part of the succession calcitization was restricted to
555 bed-margins. Samples in centres of beds, containing largely dolomite and little calcite, are most
556 easily interpreted as belonging to the least-altered carbonate samples of the Zaonega Formation,
557 and as the most likely to have preserved the $\delta^{13}\text{C}$ signal of ambient sea-water.

558
559 *5.3. Preliminary implications for the Zaonega $\delta^{13}\text{C}$ record and global Paleoproterozoic events*

560 Our results show that all studied carbonate samples have been to varying degrees affected
561 by post-depositional alteration. The least altered carbonate samples are in the centres of
562 carbonate beds composed mainly of dolomite in a tightly intergrown crystal texture and
563 containing little calcite. One current approach to identify the best-preserved carbonates within
564 the Zaonega Formation is identifying those with the highest amount of dolomite, as these are the
565 samples with the highest carbon isotope buffering capacity against secondary and subsequent
566 alterations. We have therefore used (Mg/Ca)*IC (Mg/Ca ratio multiplied by inorganic carbon) as
567 an approximation of the amount of dolomite to identify the best-preserved samples from this
568 study and those in the study of Kump et al. (2011) on the same drill core (Fig. 8b). Using our
569 (Mg/Ca)*IC metric, samples were categorized into four groups of assessed apparent alteration:
570 minor/moderate, significant, extensive, and complete (arbitrary boundaries at (Mg/Ca)*IC = 6;
571 3.5; 1; see Fig. 8b). Altogether 7 samples were found to belong to minor/moderately altered
572 category: 5 samples from the set of 39 samples of this study and 2 samples from the dataset of
573 Kump et al. (2011). We acknowledge that such a discriminatory classification is inherently
574 biased against the possibility that a few of the calcites could have well-preserved carbon isotope
575 signatures, but our aim here is solely to ascertain the samples we can be most confident about.

576 Post-depositional alteration of the Zaonega carbonate rocks is also likely indicated by
577 cross-plots of $\delta^{13}\text{C}$ and $\delta^{18}\text{O}$, as decreasing $\delta^{18}\text{O}$ values correspond to lower $\delta^{13}\text{C}$ values within
578 single beds (beds #1 and #6 in Fig. 8d). The non-primary calcites show a trend of decreasing
579 $\delta^{18}\text{O}$ values with depth, whereas the dolomites have $\delta^{18}\text{O}$ values slightly above the calcite $\delta^{18}\text{O}$
580 values (Fig. 9). Well-defined stratigraphic trend of $\delta^{18}\text{O}$ implies that the oxygen isotope
581 composition of calcite represents complete homogenization or formation during post-
582 depositional alteration and that the alteration is successively stronger down the stratigraphy (Fig.

583 9). Oxygen isotope compositions can show complete homogenization as per those beds with
584 relatively low $\delta^{18}\text{O}$ values overlapping with those of non-primary calcite (beds #2 to #5, #7, #8
585 in Fig. 8d), or they can show less modification including distinctly higher $\delta^{18}\text{O}$ values than the
586 calcite, as per beds #1 and #6 (Fig. 8d). We have therefore used values of $\delta^{18}\text{O}$ for additional
587 screening of those samples, that were found to be minor to moderately altered on the basis of
588 (Mg/Ca)*IC metric. Minor to moderately altered samples were further subdivided such that those
589 with the highest $\delta^{18}\text{O}$ were interpreted to be least altered and most likely to be archiving $\delta^{13}\text{C}$
590 values closest to the initial composition (Fig. 8d). Two out of eight studied beds contain minor to
591 moderately altered samples: the line perpendicular to the $\delta^{13}\text{C}$ vs. $\delta^{18}\text{O}$ alteration trend defines
592 the least altered sample within each carbonate bed. Both minor to moderately altered samples
593 from the data-set of Kump et al. (2011) on the basis of (Mg/Ca)*IC metric are here considered as
594 least altered carbonate samples. We have linked all the samples to the Zaonega stratigraphy (Fig.
595 9) and these show a negative $\delta^{13}\text{C}$ shift with amplitude larger than 20 ‰ (Fig. 9). Comparing
596 screened to unscreened samples shows that the difference in values between the least- to most-
597 altered is larger than 10 ‰ within the same bed or within a 20-m-thick stratigraphic interval.
598 Hence, using our selective criteria, the amplitude of the $\delta^{13}\text{C}$ shift based on un-screened samples
599 cannot be straightforwardly interpreted as a result of changes in the global carbon cycle.

600 Examining all data, those in this study and those reported by Kump et al. (2011), only
601 four carbonate samples from two stratigraphic intervals can be considered convincingly in the
602 category least altered. These samples have $\delta^{13}\text{C}$ values of +8 ‰ and +4 ‰ in the middle part of
603 the section (at 250 m and 239 m in core 12AB), and -4 ‰ and -2 ‰ at the top (at 2 m in 12AB
604 and at 58 m in 13A, respectively; Fig. 9). Thus, using our admittedly strict screening criteria,
605 least-altered $\delta^{13}\text{C}$ values define a stratigraphic profile that is considerably different from the one
606 reported previously by Kump et al. (2011) (Fig. 9). If the least altered carbonates formed in
607 equilibrium with the $\delta^{13}\text{C}$ of the global CO_2 , we can make the following conclusions about the
608 $\delta^{13}\text{C}$ of marine and atmospheric carbon at the time of deposition of the Zaonega sediments: i) i)
609 stratigraphically lowermost least-altered samples (250 and 239 m in core 12AB) have $\delta^{13}\text{C}$
610 values of +8 and +4 ‰, which are higher from that of the present; ii) among so far studied
611 carbonate samples, none is in the least-altered category in the stratigraphic interval between 239
612 m and 2 m in drillcore 12AB; conclusions about the changes in the global carbon cycle during
613 the time of deposition of this stratigraphic interval are currently not possible; and iii) the top of

614 the section is typified by $\delta^{13}\text{C}$ values of -4 ‰ and -2 ‰, which are lower from that at the present.
615 (Fig. 9).

616 Environmental conditions specific to the Paleoproterozoic Onega Basin, such as ample
617 organic matter, petroleum generation and seepage (Melezhik et al., 1999; 2009; Qu et al., 2012;
618 Strauss et al., 2013) could have influenced and lowered the $\delta^{13}\text{C}$ of the local dissolved inorganic
619 carbon pool. If the primary carbonates formed in such restricted conditions, they could reflect
620 more of a basinal than global $\delta^{13}\text{C}$ signal, whereas the non-primary carbonates should provide a
621 proxy to $\delta^{13}\text{C}$ of burial and metamorphic fluids. However, the inferred restricted basinal
622 conditions should not directly affect the isotopic composition of carbonate shedded to the
623 Zaonega basin from the shallow-water environment, which we infer as the main mechanism of
624 primary carbonate deposition based on sedimentological evidence. Much of the Zaonega
625 stratigraphy shows signs of post-depositional alteration and few least-altered samples were
626 convincingly recognized. This suggests that some primary carbonate supplied from the
627 environmentally decoupled shallower settings site might have experienced post-depositional
628 alteration in organic-rich environments in their final depositional location. We should therefore
629 apply caution when using non-discriminated $\delta^{13}\text{C}$ data of the Zaonega carbonate rocks to infer
630 functioning of the Paleoproterozoic global carbon cycle. Given these caveats, further detailed
631 sedimentological and geochemical investigations of the Zaonega rocks, as well as carbonates and
632 organic matter of other sedimentary units of similar age elsewhere, are required to corroborate
633 the existence of a major perturbation of the global carbon cycle at this time (e.g. Kump et al.
634 2011).

635

636 **6. Conclusions**

637 Based on detailed textural and geochemical characterization of representative samples from the
638 carbonate rocks of the Paleoproterozoic Zaonega Formation, Karelia, Russia, we conclude:

- 639 i) Dolomite is the early, most primary carbonate phase preserved within the
640 Zaonega Formation whereas the majority of the calcite formed during progressive
641 burial accompanied by possible hydrothermal alteration and metamorphic
642 carbonate-silicate reactions.

- 643 ii) While many studied carbonate samples have been affected by post-depositional
644 alteration, the samples most easily interpreted as least-altered contain high
645 amounts of dolomite represented by tightly-intergrown crystals, and are located in
646 the central parts of thicker carbonate beds. These yield values of $\delta^{13}\text{C}$ of 8 ‰ in
647 the middle part of the succession and decline to -4 ‰ in the topmost part.
- 648 iii) Extensive fluid circulation has permeated through the Zaonega succession causing
649 secondary calcitization of carbonate bed-margins and apparent complete
650 calcitization of some thin carbonate beds in the lowermost parts of the
651 stratigraphy close to the gabbro sill.
- 652 iv) Calcite-talc±phlogopite±actinolite mineral paragenesis suggests calcitization
653 occurring through reactions of dolomite with quartz, or possibly K-feldspar, in the
654 presence of fluids. The possibility of an initial calcitic mineralogy of carbonates
655 that might represent sedimentary layers and concretions needs further assessment.
- 656 v) When calcite and dolomite occur within the same carbonate bed, and the former is
657 significantly depleted in ^{13}C in comparison to the dolomite, this suggests the
658 formation of calcite due to infiltration of ^{13}C -depleted fluid probably sourced
659 from volcanic CO_2 and oxidation of organic matter.
- 660 vi) In most intervals, the $\delta^{13}\text{C}$ signal of the primary carbonate lithologies has been
661 variably modified such that previously published carbon isotopic profiles of the
662 Zaonega Formation based on whole rock analyses should be viewed cautiously
663 with respect to their utility in assessing the Paleoproterozoic carbon cycle.
- 664 vii) The apparent scarcity of least-altered carbonate rocks highlights the need for
665 additional study of all such units used to track the Paleoproterozoic carbon cycle
666 during the Paleoproterozoic oxidation of the Earth and the importance of careful
667 assessment for post-depositional alteration on the basis of geochemical and
668 petrographic properties.

669

670 **Acknowledgements**

671 The Norwegian Research Council grant 191530/V30 to V.A. Melezhik fully funded the work of
672 AEC, VAM and AL. ATB was supported by NERC grant NE/G00398X/1 to AEF and ARP. We
673 are grateful for sample preparation and analyses to all the personnel at NGU lab. We appreciate
674 the work on carbon and oxygen isotope analyses by Julie Dougans and Chris Taylor.
675 Arrangement of TOC, IC, and TC analyses is acknowledged to Harald Strauss.

676

677 **Appendix A. Supplementary data**

678 Supplementary data, Table A1 and A2, can be found at...

679

680 **7. References**

- 681
- 682
- 683 Al-Aasm, I.S., Taylor, B.E., South, B., 1990. Stable isotope analysis of multiple carbonate
684 samples using selective acid extraction. *Chem. Geol. (Isot. Geosci. Sect.)* 80, 119–125.
- 685
- 686 Bekker, A., Holland, H.D., Wang, P.-L., Rumble III, D., Stein, H.J., Hannah, J.L., Coetzee, L.L.,
687 Beukes, N.J., 2004. Dating the rise of atmospheric oxygen. *Nature* 427 (6970), 117–120.
- 688
- 689 Baker, A.J., Fallick, A.E., 1989. Evidence from Lewisian limestones for isotopically heavy
690 carbon in two-thousand-million-year-old sea water. *Nature* 337 (6205), 352–354.
- 691
- 692 Brasier, A.T., Fallick, A.E. Prave, A.R., Melezhik, V.A., Lepland, A., FAR-DEEP Scientists,
693 2011. Coastal sabkha dolomites and calcitised sulphates preserving the Lomagundi-Jatuli carbon
694 isotope signal. *Precambrian Research* 189, 193–211. doi:10.1016/j.precamres.2011.05.011.
- 695
- 696 Bucher, K., Frey, M., 2002. *Petrogenesis of metamorphic rocks*, Springer-Verlag, Berlin, 341 pp.
- 697
- 698 Črne, A.E, Melezhik, V.A., Prave, A.R., Lepland, A., Romashkin, A.E., Rychanchik, D.V., Hanski,
699 E.J., Luo, Zh.-Y., 2013a. 6.3.3 Zaonega Formation: FAR-DEEP Holes 12A and 12B, and
700 neighbouring quarries. In: Melezhik, V.A., Prave, A.R., Fallick, A.E., Hanski, E., Lepland, A.,
701 Kump, L.R., Strauss, H. (Eds.), *Reading the Archive of Earth's Oxygenation*, vol. 2, Springer, pp.
702 946–1007.
- 703 Črne, A.E, Melezhik, V.A., Prave, A.R., Lepland, A., Hanski, E.J., Romashkin, A.E., Rychanchik,
704 D.V., Luo, Zh.-Y., 2013b. 6.3.4 Zaonega Formation: FAR-DEEP Hole 13A. In: Melezhik, V.A.,
705 Prave, A.R., Fallick, A.E., Hanski, E., Lepland, A., Kump, L.R., Strauss, H. (Eds.), *Reading the*
706 *Archive of Earth's Oxygenation*, vol. 2, Springer, pp. 1008–1046.
- 707 Farquhar, J., Bao, H., Thiemens, M., 2000. Atmospheric Influence of Earth's Earliest Sulfur
708 Cycle. *Science* 289, 756–758.
- 709
- 710 Filippov, M.M. (Eds.), 1994. *The organic matter of Karelian Shungite rocks (Genesis, evolution*
711 *and the methods of study)*. Kola Science Centre, Petrozavodsk, 208 pp. (in Russian)
- 712
- 713 Filippov, M.M., Golubev, A.I., 1994. Carbon isotope composition of shungite rocks, In:
714 Filippov, M.M. (Eds.), *The Organic Matter of Karelian Shungite Rocks (Genesis, Evolution and*
715 *the Methods of Study)*, Karelian Research Centre, Petrozavodsk, pp. 32–43. (in Russian)
- 716
- 717 Frauenstein, F., Veizer, J., Beukes, N. Van Niekerk, H.S., Coetzee, L.L., 2009. Transvaal
718 Supergroup carbonates: Implications for Paleoproterozoic $\delta^{18}\text{O}$ and $\delta^{13}\text{C}$ records. *Precambrian*
719 *Research* 175, 149–160.
- 720
- 721 Galdobina, L.P., 1987. The Ludikovi superhorizon. In: Sokolov, V.A. (Eds.), *Geology of Karelia*,
722 *Nauka (Science)*, Leningrad, pp. 59–67. (in Russian)
- 723

- 724 Guerrero, A., Peacock, S.M., Knauth, L.P., 1997. Large ^{18}O and ^{13}C depletions in greenschist
725 facies carbonate rocks, western Arizona. *Geology* 25, 943–946.
726
- 727 Hannah, J.L., Stein, H.J., Zimmermman, A., Yang, G., Markey, R.J., Melezhik, V.A., 2006.
728 Precise 2004 ± 9 Ma Re-Os age for Pechenga black shale: comparison of sulfides and organic
729 material. *Geochemica et Cosmochimica Acta* 70, A228.
730
- 731 Hannah, J. L., Stein, H. J., Zimmerman, A., Yang, G., Melezhik, V.A., Filippov, M.M., Turgeon,
732 S.C., Creaser, R.A., 2008. Re-Os geochronology of shungite: A 2.05 Ga fossil oil field in
733 Karelia. *Geochimica et Cosmochimica Acta* 72 (12, Supplement 1), A351.
- 734 Irwin, H., Curtis, C., Coleman, M., 1977. Isotopic evidence for source of diagenetic carbonates
735 formed during burial of organic-rich sediments. *Nature* 260, 209–213.
736
- 737 Karhu, J.A., 1993. Palaeoproterozoic evolution of the carbon isotope ratios of sedimentary
738 carbonates in the Fennoscandian Shield. *Geological Survey of Finland Bulletin* 371, 1–87.
739
- 740 Karhu, J.A., Holland, H.D., 1996. Carbon isotopes and the rise of atmospheric oxygen. *Geology*
741 24, 867–870.
742
- 743 Krupenik, V.A., Akhmedov, A.M., Sveshnikova, K.Y., 2011. Isotopic composition of carbon,
744 oxygen and sulphur in the Ludicovian and Jatulian rocks. In: Glushanin, L.V., Sharov, N.V.,
745 Shchiptsov, V.V. (Eds.), *Palaeoproterozoic Onega Structure (Geology, Tectonics, Deep Structure
746 and Mineralogeny)* Karelian Research Centre, Russian Academy of Sciences, Petrozavodsk, pp.
747 250–255. (in Russian)
748
- 749 Kump, L.R., Junium, C., Arthur, M.A., Brasier, A.T., Fallick, A.E., Melezhik, V.A., Lepland, A.,
750 Črne, A.E., Luo, G., 2011. Isotopic evidence for massive oxidation of organic matter following
751 the great oxidation event. *Science* 334 (6063), 1694–1696, doi: 10.1126/science.1213999.
- 752 Lahtinen, R., Garde, A.A., Melezhik, V.A., 2008. Paleoproterozoic evolution of Fennoscandia
753 and Greenland. *Episodes* 31 (1), 9p.
754
- 755 Machel, H.G., 2000. Application of cathodoluminescence to carbonate diagenesis. In: Pagel, M.,
756 Barbin, V., Blanc, P., Ohnenstetter, D. (Eds.), *Cathodoluminescence in geosciences*, New York,
757 Springer, pp. 271–301.
758
- 759 Martin, A.P., Condon, D.J., Prave, A.R., Melezhik, V.A., Lepland, A., Fallick, A.E., 2013.
760 Dating the termination of the Palaeoproterozoic Lomagundi-Jatuli carbon isotopic event in the
761 North Transfennoscandian Greenstone Belt. *Precambrian Research* 224, 160–168.
762
- 763 Melezhik, V.A., Fallick, A.E., 1996. A widespread positive $\delta^{13}\text{C}_{\text{carb}}$ anomaly at around 2.33-2.06
764 Ga on the Fennoscandian Shield: a paradox? *Terra Nova* 8, 141-157.
765
- 766 Melezhik, V.A., Fallick, A.E., 2003. $\delta^{13}\text{C}$ and $\delta^{18}\text{O}$ variations in primary and secondary
767 carbonate phases: several contrasting examples from Palaeoproterozoic C-13-rich
768 metamorphosed dolostones. *Chemical geology* 201 (3-4), 213–228.

769
770 Melezhik, V.A., Fallick, A.E., Filippov, M.M., Larsen, O., 1999. Karelian shungite - an
771 indication of 2.0-Ga-old metamorphosed oil-shale and generation of petroleum: geology,
772 lithology and geochemistry. *Earth-Science Reviews* 47, 1–40, doi: 10.1016/S0012-
773 8252(99)00027-6.
774
775 Melezhik, V.A., Fallick, A.E., Filippov, M.M., Lepland, A., Rychanchik, D.V., Deines, Y.E.,
776 Medvedev, P.V., Romashkin, A.E., Strauss, H., 2009. Petroleum surface oil seeps from a
777 Palaeoproterozoic petrified giant oilfield. *Terra Nova* 21, 119–126, doi: 10.1111/j.1365-
778 3121.2009.00864.x.
779
780 Melezhik, V.A., Fallick, A.E., Medvedev, P.V., Makarikhin, V.V., 2000. Palaeoproterozoic
781 magnesite–stromatolite–dolostone–‘red bed’ association, Russian Karelia: palaeoenvironmental
782 constraints on the 2.0 Ga positive carbon isotope shift. *Norwegian Journal of Geology* 80, 163–
783 186.
784
785 Melezhik, V.A., Fallick, A.E., Smirnov, Y.P., Yakovlev, Y.N., 2003. Fractionation of carbon and
786 oxygen isotopes in ¹³C-rich Palaeoproterozoic dolostones in the transition from medium-grade to
787 high-grade greenschist facies: a case study from the Kola Superdeep Drillhole. *Journal of the*
788 *Geological Society* 160, 71–82.
789
790 Melezhik, V.A., Fallick, A.E., Rychanchik, D.V., Kuznetsov, A.B., 2005. Palaeoproterozoic
791 evaporates in Fennoscandia: implications for sea-water sulphate, the rise of atmospheric oxygen
792 and local amplification of the δ¹³C excursion. *Terra Nova* 17, 141–148.
793
794 Melezhik V.A., Filippov, M.M., Romashkin, A.E., 2004. A giant Palaeoproterozoic deposit of
795 shungite in NW Russia: genesis and practical applications. *Ore geology reviews* 24, 135–154.
796
797 Melezhik, V.A., Grinenko, L.N., Fallick, A.E., 1998. 2000-Ma sulphide concretions from the
798 ‘Productive’ Formation of the Pechenga Greenstone Belt, NW Russia: genetic history based on
799 morphological and isotopic evidence. *Chemical Geology* 148 (1-2), 61–94.
800
801 Melezhik, V.A., Huhma, H., Condon, D.J., Fallick, A.E., Whitehouse, M.J., 2007. Temporal
802 constraints on the Paleoproterozoic Lomagundi-Jatuli carbon isotopic event. *Geology* 35, 655–
803 658, doi: 10.1130/G23764a.1.
804
805 Melezhik, V.A., Prave, A.R., Lepland, A., Romashkin, A.E., Rychanchik, D.V., Hanski, E.J.,
806 2013. 6.3.2 Tulomozero Formation: FAR-DEEP Hole 11A. In: Melezhik, V.A., Prave, A.R.,
807 Fallick, A.E., Hanski, E., Lepland, A., Kump, L.R., Strauss, H. (Eds.), *Reading the Archive of*
808 *Earth’s Oxygenation*, vol. 2, Springer, pp. 889–945.
809
810 Morozov, A.F., Hakhaev, B.N., Petrov, O.V., Gorbachev, V.I., Tarkhanov, G.B., Tsvetkov, L.D.,
811 Erinchek, Y.M., Akhmedov, A.M., Krupenik, V.A., Sveshnikova, K.Y., 2010. Rock-salts in
812 Palaeoproterozoic strata of the Onega depression of Karelia (based on data from the Onega
813 parametric drillhole). *Transection of Academy of Sciences* 435 (2), 230–233. (in Russian)
814

815 Ovchinnikova, G.V., Kuznetsov, A.B., Melezhik, V.A., Gorokhov, I.M., Vasil'eva, I.M.,
816 Gorokhovskiy, B.M., 2007. Pb-Pb age of Jatulian carbonate rocks: the Tulomozero Formation in
817 south-eastern Karelia. *Stratigraphy and Geological Correlation* 4, 359–372.
818

819 Qu, Y., Črne, A.E., Lepland, A., van Zuilen, M., 2012. Methanotrophy in a Paleoproterozoic oil
820 field ecosystem, Zaonega Formation, Karelia, Russia. *Geobiology* 10, 467–478.
821

822 Puchtel, I.S., Arndt, N.T., Hofmann, A.W., Haase, K.M., Kroner, A., Kulikov, V.S., Kulikova,
823 V.V., Garbe-Schonberg, C.D., Nemchin, A.A., 1998. Petrology of mafic lavas within the Onega
824 plateau, central Karelia: evidence for 2.0 Ga plume-related continental crustal growth in the
825 Baltic Shield. *Contributions to Mineralogy and Petrology* 130, 134–153, doi:
826 10.1007/s004100050355.

827 Puchtel, I.S., Brugmann, G.E., Hofmann, A.W., 1999. Precise Re-Os mineral isochron and Pb-
828 Nd-Os isotope systematics of a mafic-ultramafic sill in the 2.0 Ga Onega plateau (Baltic Shield):
829 *Earth and Planetary Science Letters* 170, 447–461, doi: 10.1016/S0012-821X(99)00118-1.
830

831 Reuschel, M., Melezhik, V.A., Strauss, H., 2012. Sulfur isotopic trends and iron speciation from
832 the c. 2.0 Ga Pilgugarvi Sedimentary Formation, NW Russia. *Precambrian Research* 196, 193–
833 203, doi: 10.1016/j.precamres.2011.12.009.
834

835 Schidlowski, M., 2001. Carbon isotopes as biogeochemical recorders of life over 3.8 Ga of Earth
836 history: evolution of a concept. *Precambrian Research* 106, 117–134.
837

838 Shatsky, G.V. 1990. Isotope composition of sulphides from the Zazhogino shungite deposit.
839 *Lithology and Mineral Resources* 1, 20–28. (in Russian)
840

841 Shieh, Y.M., Taylor, H.P., 1969. Oxygen and carbon isotope studied of contact metamorphism of
842 carbonate rocks. *Journal of Petrology* 10, 307–331.
843

844 Strauss, H., Melezhik, V.A., Lepland, A., Fallick, A.E., Hanski, E.J., Filippov, M.M., Deines,
845 Y.E., Illing, C.J., Črne, A.E., Brasier, A.T., 2013. 7.6 Enhanced Accumulation of Organic
846 Matter: The Shunga Event. In: Melezhik, V.A., Kump, L.R., Fallick, A.E., Strauss, H., Hanski,
847 E., Prave, A.R., Lepland, A., (Eds.), *Reading the Archive of Earth's Oxygenation*, vol. 3,
848 Springer, pp. 1195–1273.
849

850 Valley, J.W., 1986. Stable isotope geochemistry of metamorphic rocks. In: Valley, J.W., Taylor,
851 H.P., O'Neil, J.R. (Eds.), *Stable Isotopes in High Temperature Geological Processes*. *Reviews in*
852 *Mineralogy* 16, Mineralogical Society of America, pp. 445–490.
853

854 Volodichev, O.I., 1987. Metamorphism. In: Sokolov, V.A. (Eds.), *Geology of Karelia*, Nauka,
855 Leningrad, pp. 152–175. (in Russian)
856

857 Whiticar, M.J., 1999. Carbon and hydrogen isotope systematics of bacterial formation and
858 oxidation of methane. *Chemical Geology* 161, 291–314.
859

860 Yudovich, Y.E., Makarikhin, V.V., Medvedev, P.V., Sukhanov, N.V., 1991. Carbon isotope
861 anomalies in carbonates of the Karelian Complex. *Geochemica International* 28, 56–62.

862 **Figure captions**

863 **Fig. 1.** Geological map of the Lake Onega area in central Karelia showing locations of the FAR-
864 DEEP drillholes that targeted the Zaonega Formation. The Tulomozero Formation preserves the
865 Lomagundi-Jatuli isotopic signal.

866 **Fig. 2.** Lithostratigraphic columns of the FAR-DEEP drillholes 12AB and 13A (after Črne et al.,
867 2013a,b) with marked stratigraphic positions of the carbonate beds selected for this study.

868 **Fig. 3.** Selected carbonate beds with lithological information and geochemical parameters. Beds
869 #1 and #2 are from drillhole 13A; beds #3 to #8 are from drillhole 12AB.

870 **Fig. 4.** Carbon and oxygen isotope profiles of carbonate beds #1 to #7.

871 **Fig. 5.** SEM-BSE and CL images of samples from the centres (left column) and margins (right
872 column) of carbonate beds #2 to #5 from drillholes 13A and 12AB. All scale bars show 100 μm .
873 (a) SEM-BSE image of large dolomite crystals, as much as 20 μm in size, which are zoned and
874 tightly intergrown. Overgrowing the dolomite are calcite, mica and talc; calcite occurs as
875 irregular patches of different size (centre of bed #2; sample 13A-144.27 m). (b) SEM-BSE image
876 showing calcite containing a few μm -scale rounded intercalations of quartz (marked by white
877 arrows). Also present are pyrite grains, partly overgrown by calcite. Mica is overgrowing both
878 calcite and pyrite (margin of bed #2; sample 13A-144.39 m). (c) CL image showing bright and
879 dull red luminescence of calcite (margin of bed #2; sample 144.39 m). (d) SEM-BSE image of
880 dolomite rhombohedra as large as 20 μm , which are zoned and tightly intergrown. Quartz is
881 present as dark, irregular patches in places overgrown by calcite containing spherical
882 intercalations of quartz. Calcite, mica and pyrite overgrow the dolomite (centre of bed #3;
883 sample 12B-126.88 m). (e) Large, irregular patches of calcite containing spherical intercalations
884 of quartz are overgrowing the quartz-mica matrix. Small, irregular grains of pyrite are
885 disseminated throughout the sample (margin of bed #3; sample 12B-126.52 m). (f) CL image
886 showing red luminescence of calcite, whereas dolomite, micas and pyrite are non-luminescent
887 (centre of bed #3; sample 12B-126.88 m). (g) Homogenous dolomite rhombohedra overgrown by
888 mica and calcite, the latter containing intercalations of quartz (centre of bed #4; sample 12B-
889 162.99 m). (h) Calcite, with spherical intercalations of albite (marked by white arrows),
890 overgrowing mica. Large either rectangular or irregular patches of albite overgrow mica and
891 calcite. Pyrite is present as small grains and large cubes, the latter overgrowing mica, calcite and
892 albite (margin of bed #4; sample 12B-163.13 m). (i) CL image of dull to bright red luminescent
893 calcite and dark, non-luminescent pyrite, mica and albite (margin of bed #4; sample 12B-163.13
894 m). (j) SEM-BSE image of zoned dolomite rhombohedra cemented together by dolomite cement
895 and in places surrounded by organic-matter (black) (centre of bed #5; sample 12B-183.4 m). (k)
896 SEM-BSE image of dolomite rhombohedra composed of a dark core and a bright rim, cemented
897 by large amount of homogenous dolomite cement. Some calcite containing intercalations of
898 quartz is overgrowing the dolomite. Mica overgrows both, dolomite and calcite (margin of bed
899 #5; sample 12B- 183.11 m). (l) CL image showing mostly red luminescence of rims of the

900 dolomite rhombohedra, but also some luminescent cores. The bulk of the dolomite is non-
901 luminescent (centre of bed #5; sample 12B-183.4 m).

902 **Fig. 6.** SEM-BSE and CL images of samples from the centres (left column) and margins (right
903 column) of carbonate beds #1 from drillhole 13A and #6 from drillhole 12AB. All scale bars
904 show 100 μm . (a) SEM-BSE image of mostly homogenous dolomite crystals, which are tightly
905 intergrown, with straight boundaries between the crystals. Margins of the dolomite crystals are
906 slightly brighter than the crystal cores. Minor amounts of calcite and mica are present, calcite
907 mostly occurring as irregular patches (centre of bed #1; sample 13A-58.16 m). (b) SEM-BSE
908 image of rhombohedral dolomite crystals, mostly tightly intergrown with straight contacts, but
909 also loosely packed and surrounded by organic-matter (black). A few irregular calcite patches are
910 present either overgrowing dolomite rhombohedra (lower right part of the photo) or as
911 precipitates along the dolomite crystal boundaries (margin of bed #1; sample 13A-58.45 m). (c)
912 CL image showing dull red luminescence of dolomite crystals and some bright red luminescence
913 of crystal-margins (centre of bed #1; sample 58.16 m). (d) CL image of dolomite with dull and
914 bright red zones (margin of bed #1; sample 58.45 m). (e) SEM-BSE image of homogenous
915 dolomite crystals, very tightly intergrown as indicated by sutured crystal boundaries,
916 recognizable due to their darker colour. Some mica and a few small patches of calcite are
917 present, calcite mostly along the dolomite crystals but clearly overgrowing dolomite (centre of
918 bed #6; sample 12B-249.5). (f) SEM-BSE image of quartz-rich sample containing patches of
919 calcite with spherical intercalations of quartz (margin of bed #6; sample 12B-248.7 m).

920 **Fig. 7.** SEM-BSE and CL images of samples from the centres (left column) and margins (right
921 column) of carbonate beds #7 to #8 from drillhole 12AB. All scale bars show 100 μm . (a) SEM-
922 BSE image of calcite consisting of homogenous crystals of various shapes and as much as 30 μm
923 in size, in places rhombohedra can be recognized. Albite occurs mostly as rectangular grains
924 (?replacing pyrite) but also as small intercalations of spherical shape. Some mica and small
925 titanite crystals are also present (centre of bed #7; sample 12B-283.02 m). (b) Up to 0.5 cm large
926 rhombohedra are composed of calcitic core and calcitic rim, the boundaries between the two are
927 marked by spherical intercalations of quartz; rhombohedra cores contain intercalations of albite
928 (margin of bed #7; sample 12B-282.65 m). (c) CL image of dull red to bright red luminescent
929 calcite and nonluminescent albite (centre of bed #8; sample 12B-283.02 m). (d) SEM-BSE image
930 of large, irregular calcite patches having undulating contacts with surrounding albite. Much mica
931 and some titanite are also present. Actinolite needles overgrow all mineral phases (margin of
932 bed #8; sample 12B-394.30 m).

933 **Fig. 8.** (a) Cross-plotted values of $\delta^{13}\text{C}$ and Mg/Ca ratio with separate symbols for each of the
934 studied beds. (b) Cross-plotted values of $\delta^{13}\text{C}$ and (Mg/Ca)*IC, a product between the Mg/Ca
935 ratio and inorganic carbon (IC) content, with separate symbols for each of the studied beds. Also
936 plotted are data points for samples analysed for $\delta^{13}\text{C}$ by Kump et al. (2011). Thresholds of
937 (Mg/Ca)*IC are used for approximation of sample alteration. (c) Cross-plotted values of $\delta^{13}\text{C}$
938 and IC with separate symbols for each of the studied beds. (d) Cross-plotted values of $\delta^{13}\text{C}$ and

939 $\delta^{18}\text{O}$ with separate symbols for each of the studied beds. The two minor to moderately altered
940 samples from Kump et al. (2011), recognized on the basis of $(\text{Mg}/\text{Ca})^*\text{IC}$ (Fig. 9b), are also
941 plotted. The $\delta^{13}\text{C}$ vs. $\delta^{18}\text{O}$ alteration trends for the samples located in the two beds, which
942 contain minor to moderately altered samples, are parallel and indicated by the thick grey arrows.
943 The line cutting off the least altered samples, on the basis of the data presented, is oriented
944 perpendicular to the $\delta^{13}\text{C}$ vs. $\delta^{18}\text{O}$ alteration trend.

945 **Fig. 9.** $\delta^{13}\text{C}$ and $\delta^{18}\text{O}$ values of samples from this study and the study of Kump et al. (2011)
946 plotted along the combined lithostratigraphic column of drillholes 12AB and 13A. The samples
947 are divided into four groups with different alteration grades, which correspond to the amount of
948 dolomite within the sample. The least altered carbonate samples have the largest symbols with a
949 thick black line and are denoted with an asterisk.

950